Delayed developmental maturation of frontal cortical circuits impacts decision-making

Kevin Mastro[1-3], Wen-Chun Lee[1], Wengang Wang[1], Beth Stevens[2-3], Bernardo L. Sabatini*[1-2]

1 Department of Neurobiology, Howard Hughes Medical Institute, Harvard Medical School, Boston, MA 02115, USA

2 Stanley Center at the Broad Institute at MIT and Harvard, Cambridge, MA 02139, USA

3 F. M. Kirby Neurobiology Center, Howard Hughes Medical Institute, Boston Children's Hospital, Boston, MA 02115, USA

* Correspondence: bernardo_sabatini@hms.harvard.edu

Abstract

In humans, frontal cortical circuits mature in parallel with the development of higher cognitive functions over the course of 15-20 years. In mice, behavior and brain structure change rapidly until reaching sexual maturity (~8 weeks of age). In contrast, the degree to which frontal cortices and the behaviors they support continue to develop in mice after this period is unclear. Here, we uncover age-related changes in the acquisition and execution of a probabilistic reward reinforcement task. Both young and old mice complete a similar number of trials per session, but 16-30-week-old mice obtain higher reward rates than younger mice. The older mice adjust their behavior more readily after failing to receive a reward, suggesting that age-dependent changes to circuits relevant to forming action-outcome associations, such as those in frontal associative cortices (FACs). Indeed, we identified cell-type and input-specific refinements of FAC circuits over the first 24 weeks of age, including protracted reductions in excitatory drive and increases in inhibition onto pyramidal cells. Dampening inhibitory activity in FAC alters behavior in a manner that counteracts the age-related differences. Together, these reveal an extended period of synaptic maturation in FAC that directly impacts age-related changes in decision-making.

Introduction

In humans, frontal cortical circuit maturation is a lengthy process that extends into the 2nd and 3rd decade of life and parallels the development of higher cognitive functions, such as goal-directed decision-making[1-4]. Structural changes over this time include synapse formation (birth to 10-12 years old) followed by synaptic pruning and maturation (12 to 20-25 years) and increases in myelination [5-8]. Functional imaging and physiological recordings reveal protracted changes in frontal cortical circuit connectivity and the oscillations they express that correlated with changes in behavior [9-13]. Over the same period, cognitive maturation is reflected in increased executive function and abstract reasoning and reduced impulsivity, which impact goal-directed decision-making [2, 14-18]. Moreover, perturbations of frontal cortical structure are implicated in cognitive deficits found in psychiatric and degenerative diseases [19-25].

In mice, age-dependent maturation of the circuitry of frontal association cortices (FAC) has been described up to ~8 weeks of life. Structural changes during this time include increased synapse density onto pyramidal neurons and input-specific refinement of synapses onto GABAergic interneurons [26-28]. Consistent with data from humans, lesions to mouse FAC and developmental manipulation of its inputs or local circuitry perturb cognition, including goal-directed decision-making [29-32].

Although the degree of homology of mouse and human FAC is contentious, in both species these areas are innervated by the mediodorsal thalamus (MD) [33, 34]. MD inputs are developmentally regulated, contribute to higher cognitive functions and, in mice, their manipulation affects decision-making [30, 35, 36]. Therefore, refinement of MD input may contribute to protracted development of mouse FAC and associated behavioral changes. Similarly, protracted age-dependent changes in the local GABAergic circuits, whose maturation in sensory cortical areas is thought to underlie the opening and closing of critical periods [37], may contribute to post-adolescent circuit and behavioral refinement. In sensory critical periods, fast-spiking interneurons (FSIs) constrain the developmental period (both onset and offset) and display age-dependent cellular, molecular and functional changes [38-40]. Within frontal cortical circuits, early postnatal increases in inhibition onto pyramidal neurons have been observed and developmental manipulations of FSI activity can either disrupt cognition or is a target for potential therapeutic intervention in mouse model of human disease [26, 32, 41].

59 Here, we examine the continued development of mouse FAC and behavior in FAC-dependent
60 tasks beyond the age of sexual maturity. We find differences in the acquisition and execution of
61 a FAC-dependent 2-armed bandit task (2ABT) in which thirsty mice must integrate information
62 across trials to optimally achieve water rewards. In parallel, we find changes in both FAC
63 microcircuitry and long-range excitatory inputs after the onset of sexual maturation. Utilizing
64 whole-cell electrophysiology and optogenetics in acute brain slices, we revealed that thalamic,
65 transhemispheric cortical, and local intracortical circuits continue to change after sexual maturity
66 in FAC. At sexual maturation, the relative proportions of inhibition and excitation shift towards
67 a greater influence of inhibitory tone. Furthermore, adult level performance in the 2ABT is
68 sensitive to the degree of inhibition in FAC, such that chemogenetic manipulation of FAC FSIs
69 alters how mice use past experience to select future actions. Together, these data reveal a
70 protracted period of synaptic and behavioral changes associated with the maturation of frontal
71 cortical circuits.

72

73 **Results**

74 To determine if FAC-dependent mouse behaviors change after sexual maturity, thirsty mice of a
75 variety of ages were trained in a 2-armed bandit task (2-ABT) that requires them to learn to nose
76 poke (i.e. place their snout) into a variety of ports for potential water rewards. Mice must learn
77 that one port delivers rewards at high probability and the other at low probability. The identity of
78 the highly rewarded port is held constant during "blocks" but switches in a uncued manner after
79 a predetermined number of rewards or trials (**Figure 1a**). Optimizing water acquisition on this
80 task requires the agent to infer the identity of the highly reward port based on reward history and
81 choose this port until the contingencies change. Therefore, at the start of a new block mice must
82 detect that the identity of the highly reward port has changed and adjust their behavior to
83 maximize water acquisition.

84 To learn the 2-ABT, mice progress through a curriculum of 6 learning stages that range from
85 easy to the full task**.** Mice progress from one learning stage to the next after they can acquire a
86 preset number of rewards at that stage difficulty within one session **(Supplementary Table 1)**.
87 Task acquisition is age dependent such that young mice (6-12 weeks old) move through the

88 stages more quickly and learn the full task faster than do older mice (16-30 weeks old) **(Figure**
89 **1b)**.

90 After acquiring the full task, mice progressed to the evaluation phase in which the probabilities
91 of receiving rewards are 80% on the highly rewarded port ($p_{(high\text{-}port)} = 0.8$) and 20% on the lowly
92 rewarded port ($p_{(low\text{-}port)} = 1 - p_{(high\text{-}port)} = 0.2$). Under these uncertain conditions, mice experience
93 both rewarded and unrewarded outcomes at each port throughout each block (**Figure 1c**) and
94 must integrate information across trials to determine the highly rewarded port. During the final
95 five sessions of the evaluation phase, both groups complete the same number of trials and
96 acquire a greater number of rewarded than unrewarded trials but the younger mice complete both
97 rewarded and unrewarded trials significantly faster (**Figure 1d**).

98 To assess the history dependence of behavior in the task, we examined the probability
99 that the animal selects the highly rewarded port in trials centered around the block boundaries.
100 Towards the end of one block, the behavior of mice in both age groups stabilize such that they
101 select highly rewarded port in ~2/3 of trials; however, the frequency of selected the highly
102 rewarded port is higher for mice in the older group (**Figure 1e)**. As described previously[42],
103 mice exhibit such stochastic port choice, occasionally sampling the lowly rewarded port well into
104 the block, even if the highest reward rate is theoretically achieved by consistently selected the
105 port that is inferred to be highly rewarded. At the uncued block transition, the identity of the
106 highly reward port changes and the probability of selecting it drops for both groups before
107 gradually increasing back to the steady state level (**Figure 1e**). Although mice tend to select the
108 same port on consecutive trials, they do occasionally switch port selections from trial-to-trial.
109 Older mice display greater probability of port switching than younger mice both at steady state
110 and following block transitions (**Figure 1f**). In particular, older mice are more likely to switch
111 ports after failing to receive a reward than are younger mice (i.e., they have a higher lose-switch
112 rate, **Figure 1f).** Together, these data reveal that decision-making processes change during post-
113 adolescent maturation, suggesting that concomitant changes may occur in FAC circuitry.

114 To determine the developmental profile of FAC during, we examined its circuitry and
115 synaptic properties at different ages, binning data into 4 groups depending on mouse age (2-5, 6-
116 9, 10-15, and 16-30 weeks). We performed whole-cell voltage-clamp recordings from Layer 2/3
117 (l2/3) pyramidal neurons in the prelimbic (PL) region of the FAC in acute brain slices. An

118 extracellular stimulating electrode was placed 500 µm from pia and the stimulation intensity was
119 adjusted to establish a threshold stimulus that generated a 25-250 pA excitatory response in the
120 voltage-clamped neuron (**Figure 2a-b**). For each cell, synaptic currents were recorded at holding
121 potentials of -70 and 0 mV to isolate excitatory (EPSCs) and inhibitory (IPSCs) postsynaptic
122 currents, respectively, elicited by a range of stimulus strengths relative to the minimal threshold
123 stimulus strength (**Supplementary Figure 2a-d**). Series resistance and membrane capacitance
124 were similar across groups, but membrane resistance is significantly higher at 10-15 and 16-30
125 weeks relative to other ages (**Supplementary Figure 1e**), suggesting changes in cell size and
126 passive properties across ages.

127 To compare synaptic properties across the four age groups, we normalized the amplitude
128 of evoked responses to that of the average threshold response per group which, despite our best
129 efforts, varied across the groups (**Supplementary Figure 1a-b**). Comparing the amplitude of
130 current at 1.5 the threshold stimulus strength (1.5x) revealed that this recruited the greatest
131 amount of excitatory drive at 6-9 weeks followed by 10-15 weeks as compared to all other
132 groups (**Figure 2d-e**). The amplitude of inhibitory synaptic currents evoked at this same stimulus
133 strength increased at 6-9 weeks and 10-15 weeks as compared to 2-5 weeks before decreasing
134 again at 16-30 weeks. These age-dependent changes in IPSC amplitudes were consistent across
135 the full range of stimulus strengths (**Supplementary Figure 1c-d**). Together, these data reveal
136 age-dependent reorganization of the frontal cortical circuits but what features of the circuit
137 underlie these changes remain unclear.

138 To determine whether changes in excitatory connectivity are due to pre-synaptic and/or
139 postsynaptic modifications, we measured the frequency and amplitude of spontaneous miniature
140 excitatory postsynaptic currents (mEPSCs) measured in the presence of TTX (**Figure 2f**).
141 Consistent with anatomical and electrophysiological evidence for increasing spine and synapse
142 density of l2/3 pyramidal neurons over the first 5 weeks of life [26], the frequency of mEPSCs
143 increases from postnatal 2-5 to 6-9 weeks (**Figure 2g**). However, following this peak, mEPSC
144 frequency decreases at 10-15 and 16-30 weeks (**Figure 2g**). In contrast, mEPSC amplitude
145 increases until, and is maintained after, 6-9 weeks (**Figure 2g**). The amplitude of mEPSCs
146 typically reflects post-synaptic properties such as the number of AMPA-type glutamate receptor
147 (AMPAR) per synapse, whereas changes in mEPSC frequency suggest alterations in the number
148 functional AMPAR-containing synapses due to either increases in synapse number, probability

149 of neurotransmitter release, or the fraction of synapses that contain AMPARs (i.e., that are not
150 silent) [43].

151 Mediodorsal thalamus (MD) and contralateral projecting-FAC (referred to as c-FAC)
152 send dense axonal projections that synapse onto l2/3 neurons within FAC [44]. Disturbances to
153 MD activity through lesions or prolonged inhibition perturb both physiology and behavior [30,
154 36]. MD innervates FAC early in development and the number of FAC-projecting thalamic
155 neurons decreases over early development in both humans and rodents [45, 46]. Therefore, we
156 hypothesized that changes to MD inputs may contribute to the decreases in the frequency of
157 mEPSCs and amplitude of electrically-evoked responses. To study MD inputs in isolation, we
158 stereotaxically delivered an adeno-associated virus (AAV) encoding channelrhodopsin (ChR2)
159 into MD and, 7-10 days later, prepared acute slices of FAC to examine optogenetically-evoked
160 EPSCs and disynaptic (i.e., feedforward) IPSCs in l2/3 pyramidal neurons (**Figure 3a,**
161 **Supplementary Figure 2a**). We focused on analysis of mice before (6-9 weeks) the observed
162 reduction in mEPSC frequency or after the reduction had stabilized (16-30 weeks). With the
163 highest laser power, MD-evoked EPSCs are significantly larger at 6-9 than at 16-30 weeks,
164 whereas IPSCs are unchanged (**Figure 3b-c**). These data suggest an overall decrease in the MD
165 projection strength into the l2/3 pyramidal neurons with aging.

166 c-FAC sends dense projections to Layer 3 intratelenchepalic (IT) neurons, but the
167 changes in these projections across development have not been explored. Following injections of
168 AAV driving expression of ChR2 in c-FAC, we recorded optogenetically-evoked synaptic
169 currents in l2/3 pyramidal neurons in the contralateral hemisphere (**Figure 3d, Supplementary**
170 **Figure 2b**). Optogenetic stimulation of inputs from c-FAC revealed a decrease in amplitude of
171 EPSCs across laser powers whereas inhibition was reduced at only one intensity from 6-9 to 16-
172 30 weeks (**Figure 3e-f**).

173 To investigate whether there synaptic changes are accompanied by age-related changes in
174 intrinsic properties, we obtained whole-cell current clamp recordings from l2/3 pyramidal
175 neurons and examined responses to hyper- and de-polarizing current steps (**Figure 4a-b**). In
176 response to hyperpolarizing currents, neurons from 10-15 weeks old mice had larger voltage
177 changes compared to both 6-9 weeks and 16-30 weeks **(Figure 4b, left)**. We next examined the
178 action potential characteristics at rheobase. The half-width was reduced in both 10-15 weeks and

179 16-30 weeks compared to 6-9 weeks (**Figure 4c**). Similarly, the afterhyperpolarization (AHP)
180 voltage was more hyperpolarized in 10-15 weeks as compared to the 6-9 weeks and 16-30 weeks
181 (**Figure 4b**). Consistent with this, the maximal firing was slightly increased in this age range
182 relative to both 6-9 and 16-30 weeks timepoints (**Figure 4c**). Overall, intrinsic properties of l2/3
183 pyramidal neurons are relatively similar across ages.

184 Fast-spiking interneurons (FSIs), which often express parvalbumin (PV) and
185 cholecystokinin (CCK), typically mediate the fast feedforward inhibition (FFI) in cortex,
186 including that driven by MD inputs [40, 41]. We used either a transgenic mouse (PV-cre) or an
187 adeno-associated virus engineered to express transgenes in PV neurons (E2 enhancer) to express
188 genetically-encoded fluorophores in FSIs for targeted whole-cell recordings. We used the
189 electrical stimulation protocol described above for analysis of EPSCs and IPSCs in l2/3
190 pyramidal neurons to uncover age-dependent changes in synapses formed onto FSIs (**Figure 5a**).
191 We found significant decreases in the excitatory and inhibitory drive onto superficial, putative
192 FSIs (**Figure 5b, Supplementary Figure 3a-d**) at 16-30 relative to 6-9 weeks. To delineate
193 pathway-specific changes onto FSIs, we again utilized optogenetic-assisted mapping of both MD
194 and c-FAC inputs. MD-evoked excitatory and inhibitory drive was significantly reduced at 16-30
195 compared to 6-9 weeks (**Figure 5c-d**). In contrast, the c-FAC evoked excitatory and inhibitory
196 drive were unchanged (**Figure 5e-f**). Comparing these results with the concurrently collected
197 data in l2/3 pyramidal neurons shows cell-type and pathway-specific changes over aging
198 (**Supplementary Figure 4**). MD inputs switch from more strongly innervating FSIs to equally
199 targeting FSIs and l2/3 pyramids whereas c-FAC preferentially targets FSIs at both timepoints.

200 To compare changes in excitation and inhibition across cell types, age and experimental
201 paradigm, we calculated an excitation index by dividing the amplitude of the EPSC by the sum
202 of the amplitudes of the EPSC and IPSC (referred to as R). For optogenetically-triggered
203 synaptic currents, the profile of R over age was input- and cell-type dependent: it was stable for
204 MD-evoked synaptic currents across ages whereas it increased with age for c-FAC-evoked
205 activity in FSIs and not l2/3 pyramidal cells **(Supplementary Figure 4b, d).** For electrically-
206 evoked synaptic currents onto l2/3 pyramidal neurons, IPSCs and EPSCs have similar amplitude
207 at 2-5 weeks, resulting in R~0.5. However, the excitation index decreases at 6-9 weeks before
208 increasing again in the two subsequent time periods **(Supplementary Figure 4e).** For FSIs, the
209 excitation index was ~0.5 at 6-9 weeks before first increasing at 10-15 weeks and subsequently

210 decreasing at 16-30 weeks **(Supplementary Figure 4e)**. Together, these data reveal cell-type
211 and input-specific changes in synaptic strength and in the relative contributions of excitation and
212 inhibition across age.

213 To investigate the contribution of FSI-mediated FFI to these synaptic changes, we
214 crossed the PV-*cre* mouse line with the a Cre-conditional ChR2 line (Ai32) to drive expression
215 of ChR2 in all PV cells and measured the evoked inhibitory current onto l2/3 pyramidal neurons
216 (**Figure 5g**). The light-evoked IPSC amplitude increased from 2-5 weeks to 6-9 and 10-15 weeks
217 before increasing greatly by 16-30 weeks **(Figure 5h)**. Thus, utilizing a transgenic approach for
218 ChR2 expression, reveals that local inhibitory drive from PV+ interneurons (putative FSIs)
219 undergoes a delayed period of maturation.

220 Our results demonstrate that FAC circuitry undergoes delayed development maturation,
221 including changes in long-range excitation and local inhibition that, with increasing age, result in
222 greater FSI-mediated inhibition onto l2/3 pyramidal neurons. As these circuit alterations occur
223 concurrently with changes in behavior, we examined if manipulation of inhibition in FAC
224 activity alters behavior in the 2ABT. We used an AAV driving the expression of an inhibitory
225 DREADDs receptor (hM4Di) under the enhancer element (E2) to chemogenetically target
226 putative FSIs (**Figure 6a**). Control mice were handled in the same way with the exception that an
227 E2-AAV expressing a reporter fluorophore was injected. We trained both control and hM4Di
228 expressing adult mice (16-30 weeks) without injection of DREADDs ligand until they completed
229 15 sessions and achieved expert performance (**Figure 6a**). We subsequently administered the
230 DREADDs receptor antagonist, deschloroclozapine (DCZ, 3 µg/kg) 30 minutes prior to each
231 behavioral session to both sets of mice. DCZ administration perturbed the strategy in the 2-ABT
232 in mice expressing the hM4Di construct, such that they increased their lose-switch rate. This
233 effect was seen by comparing the first two sessions with DCZ administration to the last two
234 without the drug and was specific to hM4Di expressing mice (**Figure 6b**). Thus, acute
235 manipulation of FSIs in FAC alters performance in the 2ABT, consistent with the involvement of
236 activity of these cells in this task. In order to examine the effects of prolonged changes in FSI
237 mediated inhibition on task performance, as occurs with developmental regulation of feed-
238 forward inhibition in FAC, we continue DCZ administration for an additional 8 days. In this
239 chronically manipulated state, hMD4i-expressing mice selected the highly rewarded port less

240 frequently than control mice (**Figure 6c**), recapitulating the behavioral phenotype observed in
241 young mice (**Figure 1d**).
242
243 **Discussion**
244 We find that the mouse frontal cortical circuits undergo a protracted period of maturation
245 characterized by changes in excitatory and inhibitory inputs onto l2/3 pyramidal neurons and
246 FSIs. These changes reflect pathway-specific refinements of thalamic and intracortical
247 innervation of these two cells types, as well as changes in local inhibitory circuits, during the
248 first 6 months of life. Behaviorally, we find age-related differences in both the acquisition and
249 execution of a probabilistic 2-ABT over the same period such that 6-12 week old mice acquire
250 the task more quickly than their 16-30 week old counterparts. After task acquisition, the older
251 mice are more likely to both select the highly reward port and to switch between ports trial-to-
252 trial, reflected differences in task execution. Chemogenetic inhibition of FSIs in 16-30 week old
253 mice acutely and chronically alters behavior in the 2ABT. Furthermore, chronic inhibition
254 results in task performance in older mice that resembles that of 6-12 weeks old mice. Thus,
255 refinement of FAC inhibition contributes to age-related changes in behavior and to the prolonged
256 development of the FAC circuits.
257
258 *Cortical inhibition regulates plasticity and cognitive behaviors*
259 Periods of heightened plasticity, known as critical periods, have been extensively studied in
260 sensory areas where modulation of inhibition is postulated to open and close plasticity windows
261 [39]. Furthermore, experience-dependent refinement of GABAergic circuits is coordinated
262 across multiple inhibitory cell-types and is necessary to establish the precise wiring of cortical
263 circuits. Specifically, FSIs and low-threshold spiking interneurons (LTSI) establish their
264 connectivity at different rates and their post-natal maturation has been observed across multiple
265 sensory areas [47-50]. We show with electrical stimulation that FAC inhibitory circuits continue
266 to refine in a complex manner over a prolonged 30-week period, with increases in evoked
267 inhibition at 6-15 weeks of age relative to younger and older ages. In contrast, selective
268 activation of PV-mediated inhibition shows that the inhibition of l2/3 pyramidal neurons by FSIs

269 increases steadily across this same period. These data suggest that continued maturation of other
270 inhibitory circuits also occurs, including potentially that mediated by LTSIs.

271 Similar changes occur during the protracted development of human frontal cortex, which
272 includes decreases in excitation and increases in GABA-mediated inhibition until excitatory and
273 inhibitory ratios stabilize in adulthood [51, 52]. Greater inhibitory tone has been postulated to
274 contribute to the refinement of higher cognitive functions. Nevertheless, the specific cellular and
275 synaptic changes that results in the correct excitatory and inhibitory drives at the levels of
276 individual cells and the whole circuits are not fully understood.

277

278 *Age impacts decision making*

279 Following sensory critical periods, the brain continues to develop and refine into adulthood,
280 which impacts decision making in humans and rodents [2, 54]. In these species, the maturation of
281 frontal cortical circuits has been linked to behavioral changes and lesions of specific frontal
282 circuits perturb decision-making. From an evolutionary perspective, the frontal cortex has
283 undergone the greatest expansion within mammals and is most complex and enlarged in
284 primates. Although rodent frontal cortex lacks the regionalization and some of the anatomical
285 attributes (e.g., granularity) found in humans, there are anatomical and functional parallels. First,
286 rodent frontal cortex has a similar pattern of connectivity with thalamus and other subcortical
287 regions as primate frontal cortex. Second, lesions to distinct regions perturb decision-making.
288 Lastly, consistent with observations in humans, changes to frontal cortical structure and function
289 are implicated in the modulation of decision-making during development, diseases and
290 degeneration.

291 The data presented here illuminate the complex changes that occur in one part of mouse
292 FAC circuitry over a protracted developmental period and that influence the relative activation of
293 inhibitory and excitatory cortical neurons. However, they likely comprise only a small part of
294 the circuity changes that occur over this period. In addition to the inputs from MD and c-FAC,
295 FAC is innervated by other cortical areas, ventromedial thalamus, amygdala, hippocampus and
296 VTA. Moreover, the FAC contains additional laminar organization and a diverse set of
297 interneurons which likely also change over this extended period. In addition, both the refinement
298 and action of neuromodulators, including dopamine, likely contribute to post-sexual maturity

circuit development, as occurs in the maturation of human FAC and reward processing systems. Therefore, cell-type and input-specific chemogenetic manipulation of FAC FSIs, such as done here, is unlikely to fully revert the behavior of an aged animal to that of a younger one. Nevertheless, it does demonstrate the sufficiency of changes in the activity or synapses of specific interneuron population, such as we find occurs during protracted FAC development, to influence complex behaviors. Our data reveal that blunting FAC inhibition does not influence all aspects of 2ABT behavior but does modulates switching behavior following a negative outcome. In future experiments, will address the contribution of other circuit elements to age-dependent changes in cognitive behaviors in mice.

Linking synapses to behavior: implications for aging

The synaptic and circuit changes demonstrated here are likely driven by age-dependent transcriptional, neuromodulatory, and experience-dependent processes in both neuronal and non-neuronal cells. Microglial and astrocytic pruning of synapses are key candidates for the mechanisms of developmental circuit sculpting. In addition, oligodendrocytes contribute via post-adolescence myelination including in frontal cortex (FC) which is one of the last brain regions to myelinate. These programs likely also contribute to neuropsychiatric disease, including schizophrenia and other disorders that typically manifest during the transition from adolescence to adulthood and whose risk factors include genes involved in synaptic, glial, and neuroimmune pathways [55-57]. However, further characterization of developmental and disease associated circuit changes, as well as quantitative models in which to examine the functional implications of these alterations, are necessary to understand their full contribution to normal aging and disease progression.

Methods

All procedures were performed in accordance with the guidelines established by the National Institutes of Health and with approval from the Harvard Medical School Institutional Animal Care and Use Committee.

328 **Animals**

329 Male mice ranging from 2-30 weeks old on the C57BL/6J (Strain #:000664) background from
330 Jackson Laboratory were employed for all studies. To target a fluorophore or opsin to
331 parvalbumin-positive interneurons, we crossed the PV-Cre (Strain #: 017320) to Ai14 (dTomato,
332 Strain #:007914) or Ai32 (ChR2: Strain #:024109) mouse lines, respectively.

333

334 **Viruses**

335 Recombinant adeno-associated viruses (AAVs with stereotypes 2/9, 5 and PHP.eB) were used to
336 identify, monitor or manipulate cell-types utilized viral strategies in the C57BL6/Jax (Strain
337 #:000664) mouse cohort via neuronal or PV-specific enhancer elements[58]. Most viral plasmids
338 can be found at Addgene: AAV5-CamKII-GCaMP6f-WPRE-SV40 (no. 100834-AAV5), AAV9-
339 hSyn-hChR2(H134R)-EYFP (no. 26973-AAV9), and AAV-PHP.eB-S5E2-dTom-nlsdTom (no.
340 135630-PHPeB). Some custom plasmids were packaged commercially (WZ Biosciences): AAV-
341 PHP.eB-S5E2-hM4D(Gi)-mCherry. The E2-enhancer element provided directed expression in
342 putatively parvalbumin-positive interneurons in frontal association cortex[58]. Upon delivery,
343 viruses were separated into single-use aliquots (3-5 uL) and stored in the -80ºC. Injection
344 volumes ranged from 200-250nL and titers were adjusted to approximately 10^{11} to 10^{12} genomic
345 copies per ml.

346

347 **Surgery**

348 Stereotaxic injections were performed similarly to previously reported studies[59]. Briefly, mice
349 were anesthetized deeply using isoflurane before being placed in a stereotaxic frame where body
350 temperature and level of anesthesia were monitored throughout the procedure. For all surgeries,
351 the skull was exposed and the distance from bregma to lambda was used to both level and
352 normalized for changes in skull size over the lifespan (normalization factor = measured distance
353 (mm) /4.2 mm). Coordinates were established from bregma and a drill was used to make small
354 craniotomies for viral injections. We used the following coordinates used for each brain area:
355 prelimbic region of the FAC (Area 24: A/P = +1.85, M/L = +/- 0.40, D/V = -1.85) and
356 mediodorsal thalamus (MD: A/P = -1.3, M/L = +/- 0.55 , D/V = -3.05). Pulled electrodes

containing the virus would be slowly lower to the dorsal/ventral coordinate and allowed to sit for 5 minutes. Infusion of the virus took 4-5 minutes at a rate of 50 nl/min and was followed by an additional 5 mins to counteract any flow up the injection site. After completing the injections, skin was returned and sutured and ointment was used to prevent any infection and limit inflammation.

Behavior

The two-armed bandit task (2-ABT) was consistent in both box and behavioral design as previous work[42, 59]. Briefly, mice were water regulated to 1-2 ml/day until they maintained ~80% *ad libitum* weight. On training days, mice were placed in a 4.9" x 6" acrylic chamber that contained three custom nose ports with an infrared-beam sensor (full design plans can be found on "Open Behavior").

To facilitate the acquisition of the task, mice progressed through a series of stages. As shown in **Supplementary Table 1**, parameters of the tasks were shifted until achieving the ideal task structure where decisions are made within 2 seconds ("Decision Window") where the probability of the highly rewarded port ("p(high port)") was 0.8, probability of the low rewarded port ("p(low port)") was 0.2 with a variable blocklength of 10-30 trials. For example, Stage 1 rewards the agent for any pokes in the right and left ports. This stage is necessary to acquire the relationship between a nose poke action and the reward. Stage 2 requires the agent to poke in the center port followed by side port poke and reward. This center to side association is strengthened through a combination of decreasing the amount of time allowed between the two pokes (Stage 2-5) followed by a reduction in the length of a given block (Stage 6). To complete a stage, animals had to successfully acquire 100 rewards in a given session for each of stages 1-5 and 200 rewards for Stage 6. Upon successful acquisition of the task, mice were progressed to stage 7 where they completed 8-12 sessions of the probabilistic task. Behavioral training was completed during the dark phase of the mouse sleep/wake cycle and were run under no ambient light.

Behavioral Analysis

386 All metrics were based on completed trials where mice initiated a center nose poke followed by
387 the selection of a right or left nose poke. To observe differences in training, the number of days
388 to achieve criterion on any given stage was plotted.

389 To evaluate the performance on the probabilistic task, the probability that a mouse selects the
390 highly reward port can be calculated relative to the trial position in the block. At 'Block Position'
391 zero, the highly rewarded port switches to the other port (From left to right, or right to left) and
392 the mouse must adapt their behavior to track the change in the task. The action of the mouse can
393 be represented by either the probability of correctly choosing the highly-rewarded port (p(high
394 port)) or the probability of switching (p(switch)) which would be expected to increase after block
395 position 0.

396 We employed a bootstrapping approach to estimate the means and standard deviations of several
397 behavioral metrics across conditions or age groups. For each metric, data was resampled with
398 replacement 500 times to generate bootstrapped distributions. To quantify the differences
399 between conditions, we calculated the delta (Δ) values by subtracting the bootstrapped estimates
400 of the control group from those of the treatment group for each iteration (p120-180 vs p60-100 or
401 Control vs hM4Di, respectively). This generated a distribution of delta values, representing the
402 pairwise differences between the two groups.

403

404 **Slice physiology preparation**

405 Coronal sections (250-300 um thickness) were prepared from brains of 5-28 weeks-old mice.
406 First, mice were transcranially perfused with ice-cold ACSF solution (in mM): 125 NaCl,
407 2.5 KCl, 25 NaHCO3, 2 CaCl2, 1 MgCl2, 1.25 NaH2PO4 and 11 glucose (300–
408 305 mOsm kg−1). Slices from the anterior portion of the mouse brain that contained prelimbic
409 region of the FAC were prepared on a Leica VT1200 vibratome in the same ice-cold ACSF
410 solution followed by a 5-10 min incubation period at 34 °C containing a choline-based solution
411 (in mM): 110 mM choline chloride, 25 mM $NaHCO_3$, 2.5 mM KCl, 7 mM $MgCl_2$, 0.5 mM
412 $CaCl_2$, 1.25 mM NaH_2PO_4, 25 mM glucose, 11.6 mM ascorbic acid and 3.1 mM pyruvic acid.
413 The choline-based incubation is followed by an additional 15-minute incubation in ACSF at
414 34 °C. After the second incubation, slices were moved to room temperature and maintained for

415 the length of the recording. All solutions were carbogenated at all stages of tissue preparation
416 and data collection.

417

418 **Slice physiology collection and analysis**

419 General recording principals: Recordings were made at 32-34°C in carbogenated ACSF (in mM):
420 125 NaCl, 26 NaHCO3, 1.25 NaH2PO4, 2.5 KCl, 12.5 glucose, 1 MgCl2, and 2 CaCl2. Data
421 was collected on and a low-pass filter was applied (MultiClamp 700B amplifier; Molecular
422 Devices) and then digitized on a National Instruments acquisition board. Data was acquired via a
423 custom version of ScanImage written in MATLAB. Data was analyzed offline using custom
424 code written in Matlab or Python. Electrodes were made from borosilicate glass (pipette
425 resistance, 2– 4 M). Series resistance was monitored throughout the voltage clamp recordings
426 and prior to the start of all current clamp recordings and cells were excluded if series changed
427 greater than 20% of the initial baseline.

428

429 Voltage clamp recordings utilized a cesium-based internal (in mM): 135 $CsMeSO_3$, 10 HEPES, 1
430 EGTA, 3.3 QX-314 (Cl^- salt), 4 Mg^-ATP, 0.3 Na-GTP, 8 Na_2-phosphocreatine, pH 7.3 adjusted
431 with CsOH; 295 mOsm kg^-1). For the external ACSF solution for the electrical and optogenetic
432 experiments, no blockers were used in the external ACSF. For miniature excitatory postsynaptic
433 (mEPSC) experiments, external ACSF contained 1 μM TTX and 10 uM CPP. Voltage-clamp
434 recordings were filtered at 2 kHz and digitized at 10 kHz.

435 For mEPSC recordings, cells were held at -70 mV and monitored for 5-10 mins. Recording
436 epochs with stable baselines and access resistance were included for analysis. To measure the
437 frequency and amplitude of the excitatory events, we utilized custom MATLAB scripts adapted
438 [60]and applied previously[61].

439 For electrical stimulation, a bipolar concentric electrode was positioned 500 um from the top of
440 pia and recordings targeted superficial pyramidal neurons and putative fast-spiking interneurons
441 labeled by either viral or transgenic approaches. As described previously[62], threshold (theta)
442 was established by tuning the electrical stimulation (1 pulse @ 10 ms) until a 20-150 pA (peak
443 magnitude) excitatory postsynaptic current was present at the -70 mV holding voltage. The

threshold was then multiplied by 1.1-1.5 and responses were recorded at both -70 mV and 0 mV for each neuron. Each stimulation intensity was collected five times with a 30 second inter-stimulation interval. For optogenetic stimulation, laser power was calibrated to the same level of laser intensity. Stimulation (1 pulse @ 3 ms) were taken at varying laser intensities and were randomly interspersed. Each laser intensity was collected three times with a 30 second inter-stimulation interval. Like electrical stimulation, cells were held at -70 mV (to isolate excitatory drive) followed by 0 mV hold (to isolate inhibitory drive). To understand how each stimulation impacted the local network, the current response for each stimulation was integrated over a 20 ms window of time (Area under the curve). To isolate the impact of monosynaptic drive, peak magnitude was analyzed within a short latency activation (<5 ms). For statistical testing, multiple unpaired t-tests adjusted for multiple comparisons were performed and both the p-value and q-value (adjusted for False Discovery Rate) are reported.

Currently clamp recordings utilized a potassium-based internal: 130 KMeSO3, 3 KCl, 10 HEPES, 1 EGTA, 4 Mg-ATP, 0.3 Na-GTP, 8 sodium phosphocreatine (pH 7.3 adjusted with KOH; 295 mOsm). For recordings of intrinsic excitability, 10 uM gabazine 10 uM NBQX and 10 uM CPP were included in the bath to block fast inhibitory and excitatory transmission, respectively. Data was filtered at 10 kHz and digitized at 40 kHz. Each step included a -100 pA step for 100 ms for the calculation of input resistence. For current-voltage relationship, current steps were applied for 1000 ms from -200 to 200 pA in 20 pA steps. For current-firing rate relationship, additional steps were applied from 200-1500 pA in 50-100 pA steps. Cells were monitored for inactivation and steps following inactivation were excluded from analysis.

Behavioral Chemogenetics

Mice underwent surgery and were randomly assigned to receive injection of HM4Di or mCherry viral vectors. Following surgical recovery and water regulation, mice completed acquisition (Stages 1-6) and 15 sessions of the probabilistic (Stage 7) of the 2-ABT. After which animals were administered the DREADDs activator deschloroclozapine (DCZ: 1-3 mg/ml) via intraperitoneal injection 30-minutes prior to completing the task for 10 sessions [63]. Experimenters were blind to experimental conditions during data acquisition.

474

475 **Histology and Imaging**

476 Mice were deeply anesthetized with isoflurane and perfused transcardially with 20 ml of PBS
477 followed by 10 ml of 4% paraformaldehyde (PFA). Brain was excavated and placed overnight in
478 4% PFA at 4ºC. Brains were transferred to 30% sucrose for equilibration and stored at 4ºC until
479 falling to the bottom of the container. Using dry ice, brains were frozen in an optimal cutting
480 temperature compound (O.C.T.: Tissue-Tek) and cut on the cryostat (50 um slice). DAPI
481 mounting medium (Vectashield, H-1200) was used to preserve fluorescence quality and was
482 imaged immediately on a widefield microscope at 10x objective. For viral verification, no
483 enhancement of the expression was necessary.

484

485 **Statistics**

486 Statistical analysis was completed using custom MATLAB and Python scripts and Prism
487 (GraphPad; Version 10).

488

489

490

491

492

493

494

495

496

497

498

499

References

1. Spear, L.P., *The adolescent brain and age-related behavioral manifestations.* Neuroscience & biobehavioral reviews, 2000. **24**(4): p. 417-463.
2. Tervo-Clemmens, B., et al., *A canonical trajectory of executive function maturation from adolescence to adulthood.* Nature communications, 2023. **14**(1): p. 6922.
3. Larsen, B. and B. Luna, *Adolescence as a neurobiological critical period for the development of higher-order cognition.* Neurosci. Biobehav. Rev., 2018. **94**: p. 179-195.
4. Luna, B., A. Padmanabhan, and K. O'Hearn, *What has fMRI told us about the development of cognitive control through adolescence?* Brain Cogn., 2010. **72**(1): p. 101-113.
5. Miller, D.J., et al., *Prolonged myelination in human neocortical evolution.* Proc Natl Acad Sci U S A, 2012. **109**(41): p. 16480-5.
6. Giorgio, A., et al., *Longitudinal changes in grey and white matter during adolescence.* Neuroimage, 2010. **49**(1): p. 94-103.
7. Huttenlocher, P.R., *Synaptic density in human frontal cortex - developmental changes and effects of aging.* Brain Res, 1979. **163**(2): p. 195-205.
8. Petanjek, Z., et al., *The Protracted Maturation of Associative Layer IIIC Pyramidal Neurons in the Human Prefrontal Cortex During Childhood: A Major Role in Cognitive Development and Selective Alteration in Autism.* Front Psychiatry, 2019. **10**: p. 122.
9. Candelaria-Cook, F.T., et al., *Developmental trajectory of MEG resting-state oscillatory activity in children and adolescents: a longitudinal reliability study.* Cerebral Cortex, 2022. **32**(23): p. 5404-5419.
10. Liuzzi, L., et al., *Changes in behavior and neural dynamics across adolescent development.* J. Neurosci., 2023. **43**(50): p. 8723-8732.
11. Whitford, T.J., et al., *Brain maturation in adolescence: concurrent changes in neuroanatomy and neurophysiology.* Hum. Brain Mapp., 2007. **28**(3): p. 228-237.
12. Calabro, F.J., et al., *Development of hippocampal–prefrontal cortex interactions through adolescence.* Cerebral Cortex, 2020. **30**(3): p. 1548-1558.
13. Tang, L., A.T. Shafer, and N. Ofen, *Prefrontal cortex contributions to the development of memory formation.* Cerebral Cortex, 2018. **28**(9): p. 3295-3308.
14. Cromer, J.A., et al., *The nature and rate of cognitive maturation from late childhood to adulthood.* Frontiers in psychology, 2015. **6**: p. 127486.
15. Luciana, M., et al., *The development of nonverbal working memory and executive control processes in adolescents.* Child development, 2005. **76**(3): p. 697-712.
16. Luna, B., et al., *Maturation of cognitive processes from late childhood to adulthood.* Child development, 2004. **75**(5): p. 1357-1372.
17. Ordaz, S.J., et al., *Longitudinal growth curves of brain function underlying inhibitory control through adolescence.* Journal of Neuroscience, 2013. **33**(46): p. 18109-18124.
18. Quach, A., et al., *Adolescent development of inhibitory control and substance use vulnerability: A longitudinal neuroimaging study.* Developmental cognitive neuroscience, 2020. **42**: p. 100771.
19. Flynn, S.W., et al., *Abnormalities of myelination in schizophrenia detected in vivo with MRI, and post-mortem with analysis of oligodendrocyte proteins.* Mol Psychiatry, 2003. **8**(9): p. 811-20.
20. Glantz, L.A. and D.A. Lewis, *Reduction of synaptophysin immunoreactivity in the prefrontal cortex of subjects with schizophrenia. Regional and diagnostic specificity.* Arch Gen Psychiatry, 1997. **54**(10): p. 943-52.
21. Glantz, L.A. and D.A. Lewis, *Dendritic spine density in schizophrenia and depression.* Arch Gen Psychiatry, 2001. **58**(2): p. 203.

22. Goto, Y., C.R. Yang, and S. Otani, *Functional and dysfunctional synaptic plasticity in prefrontal cortex: roles in psychiatric disorders.* Biological psychiatry, 2010. **67**(3): p. 199-207.
23. Kumari, V., et al., *Cortical grey matter volume and sensorimotor gating in schizophrenia.* Cortex, 2008. **44**(9): p. 1206-14.
24. Li, M., C. Long, and L. Yang, *Hippocampal-prefrontal circuit and disrupted functional connectivity in psychiatric and neurodegenerative disorders.* BioMed research international, 2015. **2015**.
25. Narayanan, M., et al., *Common dysregulation network in the human prefrontal cortex underlies two neurodegenerative diseases.* Molecular systems biology, 2014. **10**(7): p. 743.
26. Kroon, T., et al., *Early postnatal development of pyramidal neurons across layers of the mouse medial prefrontal cortex.* Sci Rep, 2019. **9**(1): p. 5037.
27. Caballero, A., et al., *Differential regulation of parvalbumin and calretinin interneurons in the prefrontal cortex during adolescence.* Brain Structure and Function, 2014. **219**: p. 395-406.
28. Caballero, A., et al., *Emergence of GABAergic-dependent regulation of input-specific plasticity in the adult rat prefrontal cortex during adolescence.* Psychopharmacology, 2014. **231**: p. 1789-1796.
29. Bissonette, G.B., et al., *Double dissociation of the effects of medial and orbital prefrontal cortical lesions on attentional and affective shifts in mice.* Journal of Neuroscience, 2008. **28**(44): p. 11124-11130.
30. Benoit, L.J., et al., *Adolescent thalamic inhibition leads to long-lasting impairments in prefrontal cortex function.* Nature neuroscience, 2022. **25**(6): p. 714-725.
31. Ferguson, B.R. and W.-J. Gao, *Thalamic control of cognition and social behavior via regulation of gamma-aminobutyric acidergic signaling and excitation/inhibition balance in the medial prefrontal cortex.* Biological psychiatry, 2018. **83**(8): p. 657-669.
32. Canetta, S.E., et al., *Mature parvalbumin interneuron function in prefrontal cortex requires activity during a postnatal sensitive period.* Elife, 2022. **11**: p. e80324.
33. Laubach, M., et al., *What, if anything, is rodent prefrontal cortex?* eneuro, 2018. **5**(5).
34. Le Merre, P., S. Ährlund-Richter, and M. Carlén, *The mouse prefrontal cortex: Unity in diversity.* Neuron, 2021. **109**(12): p. 1925-1944.
35. Ferguson, B.R. and W.-J. Gao, *Development of thalamocortical connections between the mediodorsal thalamus and the prefrontal cortex and its implication in cognition.* Frontiers in human neuroscience, 2015. **8**: p. 1027.
36. Ouhaz, Z., et al., *Mediodorsal thalamus is critical for updating during extradimensional shifts but not reversals in the attentional set-shifting task.* Eneuro, 2022. **9**(2).
37. Le Magueresse, C. and H. Monyer, *GABAergic interneurons shape the functional maturation of the cortex.* Neuron, 2013. **77**(3): p. 388-405.
38. Reh, R.K., et al., *Critical period regulation across multiple timescales.* Proc. Natl. Acad. Sci. U. S. A., 2020. **117**(38): p. 23242-23251.
39. Hensch, T.K., *Critical period plasticity in local cortical circuits.* Nat. Rev. Neurosci., 2005. **6**(11): p. 877-888.
40. Takesian, A.E. and T.K. Hensch, *Balancing plasticity/stability across brain development.* Prog. Brain Res., 2013. **207**: p. 3-34.
41. Mukherjee, A., et al., *Long-lasting rescue of network and cognitive dysfunction in a genetic schizophrenia model.* Cell, 2019. **178**(6): p. 1387-1402. e14.
42. Beron, C.C., et al., *Mice exhibit stochastic and efficient action switching during probabilistic decision making.* Proc Natl Acad Sci U S A, 2022. **119**(15): p. e2113961119.

43. Vardalaki, D., K. Chung, and M.T. Harnett, *Filopodia are a structural substrate for silent synapses in adult neocortex.* Nature, 2022. **612**(7939): p. 323-327.
44. Little, J.P. and A.G. Carter, *Subcellular synaptic connectivity of layer 2 pyramidal neurons in the medial prefrontal cortex.* J Neurosci, 2012. **32**(37): p. 12808-19.
45. Abitz, M., et al., *Excess of neurons in the human newborn mediodorsal thalamus compared with that of the adult.* Cerebral Cortex, 2007. **17**(11): p. 2573-2578.
46. Rios, O. and J. Villalobos, *Postnatal development of the afferent projections from the dorsomedial thalamic nucleus to the frontal cortex in mice.* Developmental brain research, 2004. **150**(1): p. 47-50.
47. Tuncdemir, S.N., et al., *Early somatostatin interneuron connectivity mediates the maturation of deep layer cortical circuits.* Neuron, 2016. **89**(3): p. 521-535.
48. Takesian, A.E., V.C. Kotak, and D.H. Sanes, *Presynaptic GABA(B) receptors regulate experience-dependent development of inhibitory short-term plasticity.* J. Neurosci., 2010. **30**(7): p. 2716-2727.
49. Bartley, A.F., et al., *Differential activity-dependent, homeostatic plasticity of two neocortical inhibitory circuits.* J. Neurophysiol., 2008. **100**(4): p. 1983-1994.
50. Miao, Q., et al., *Selective maturation of temporal dynamics of intracortical excitatory transmission at the critical period onset.* Cell Rep., 2016. **16**(6): p. 1677-1689.
51. McKeon, S.D., et al., *Prefrontal excitation/ inhibition balance supports adolescent enhancements in circuit signal to noise ratio.* bioRxivorg, 2024.
52. Perica, M.I., et al., *Development of frontal GABA and glutamate supports excitation/inhibition balance from adolescence into adulthood.* Prog. Neurobiol., 2022. **219**(102370): p. 102370.
53. Xue, M., B.V. Atallah, and M. Scanziani, *Equalizing excitation–inhibition ratios across visual cortical neurons.* Nature, 2014. **511**(7511): p. 596-600.
54. Shoji, H., et al., *Age-related changes in behavior in C57BL/6J mice from young adulthood to middle age.* Mol. Brain, 2016. **9**: p. 11.
55. Baum, M.L., et al., *CSMD1 regulates brain complement activity and circuit development.* Brain, Behavior, and Immunity, 2024. **119**: p. 317-332.
56. Sekar, A., et al., *Schizophrenia risk from complex variation of complement component 4.* Nature, 2016. **530**(7589): p. 177-183.
57. Singh, T., et al., *Rare coding variants in ten genes confer substantial risk for schizophrenia.* Nature, 2022. **604**(7906): p. 509-516.
58. Vormstein-Schneider, D., et al., *Viral manipulation of functionally distinct interneurons in mice, non-human primates and humans.* Nat Neurosci, 2020. **23**(12): p. 1629-1636.
59. Chantranupong, L., et al., *Dopamine and glutamate regulate striatal acetylcholine in decision-making.* Nature, 2023. **621**(7979): p. 577-585.
60. Merel, J., et al., *Bayesian methods for event analysis of intracellular currents.* J Neurosci Methods, 2016. **269**: p. 21-32.
61. Wilton, D.K., et al., *Microglia and complement mediate early corticostriatal synapse loss and cognitive dysfunction in Huntington's disease.* Nat Med, 2023. **29**(11): p. 2866-2884.
62. Antoine, M.W., et al., *Increased Excitation-Inhibition Ratio Stabilizes Synapse and Circuit Excitability in Four Autism Mouse Models.* Neuron, 2019. **101**(4): p. 648-661 e4.
63. Nagai, Y., et al., *Deschloroclozapine, a potent and selective chemogenetic actuator enables rapid neuronal and behavioral modulations in mice and monkeys.* Nat Neurosci, 2020. **23**(9): p. 1157-1167.

Figure 1

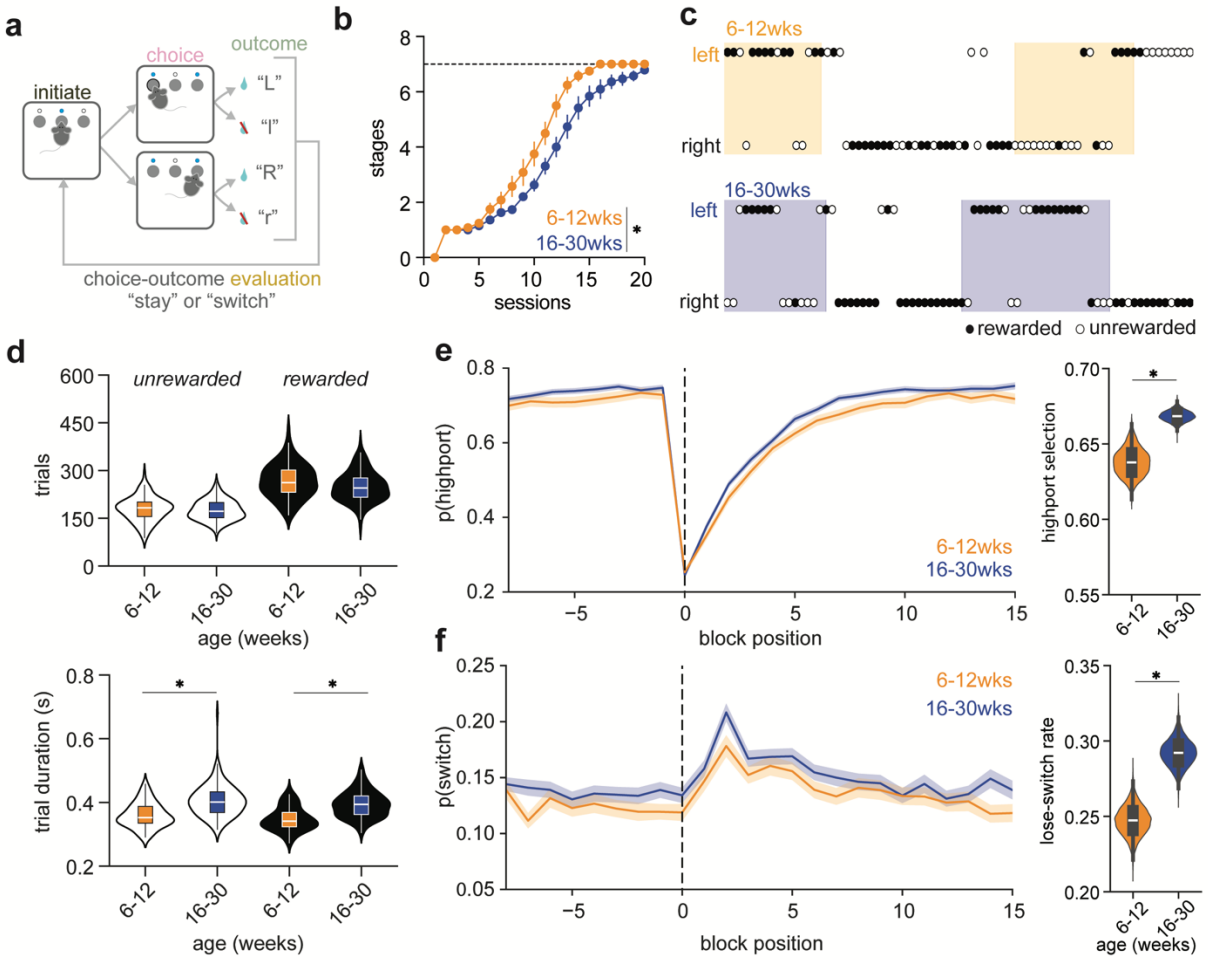

Figure 1. Age related differences in acquisition and execution of a 2-armed bandit task

a, Schematic representation of task structure. Mice initiate a trial with a nose poke in the center port followed by a side choice selection whose outcome is probabilistic delivery of a water reward. The identity of the highly rewarded port is held constant for a variable length of rewards during acquisition or trials during evaluation (known as a 'block') before the rule is reversed.

b, Proportion of mice progressing from stage 1 to 7 across daily sessions of training (~30 mins/session) across two ages ($n_{6\text{-}12wks}$=12 & $n_{16\text{-}30wks}$=18 mice). Two-way repeated measures ANOVA was performed (p=0.001).

c, Schematic representation of task performance showing that mice select the left (top) or right (bottom) port which is followed by either a rewarded (filled) or unrewarded (unfilled) outcome. Shaded portions show the blocks in which the left port is highly rewarded.

d, Boxplots superimposed onto violin plots of the number of trials completed per session (top) and trial duration (bottom) that are either rewarded (filled) or unrewarded (unfilled) during the evaluation phase. Student's T-test comparing rewarded and unrewarded across age groups (p=0.001).

e, Probability of selecting the highly rewarded port (p(high-port)) at each trial position before (-5 to -1), after (1-12) the rule change (block position=0) (*left*) and violin plot of the bootstrapped probability distributions for selecting the highly rewarded port (*right*) ($p<0.0001$).

f, Probability of switching the selected side choice (p(switch)) at each trial position before (-5 to -1), after (1-12) the rule change (block position=0) (*left*) and violin plot of the bootstrapped probability distributions for switch ports after a loss (*right*) ($p<0.0001$).

Figure 2

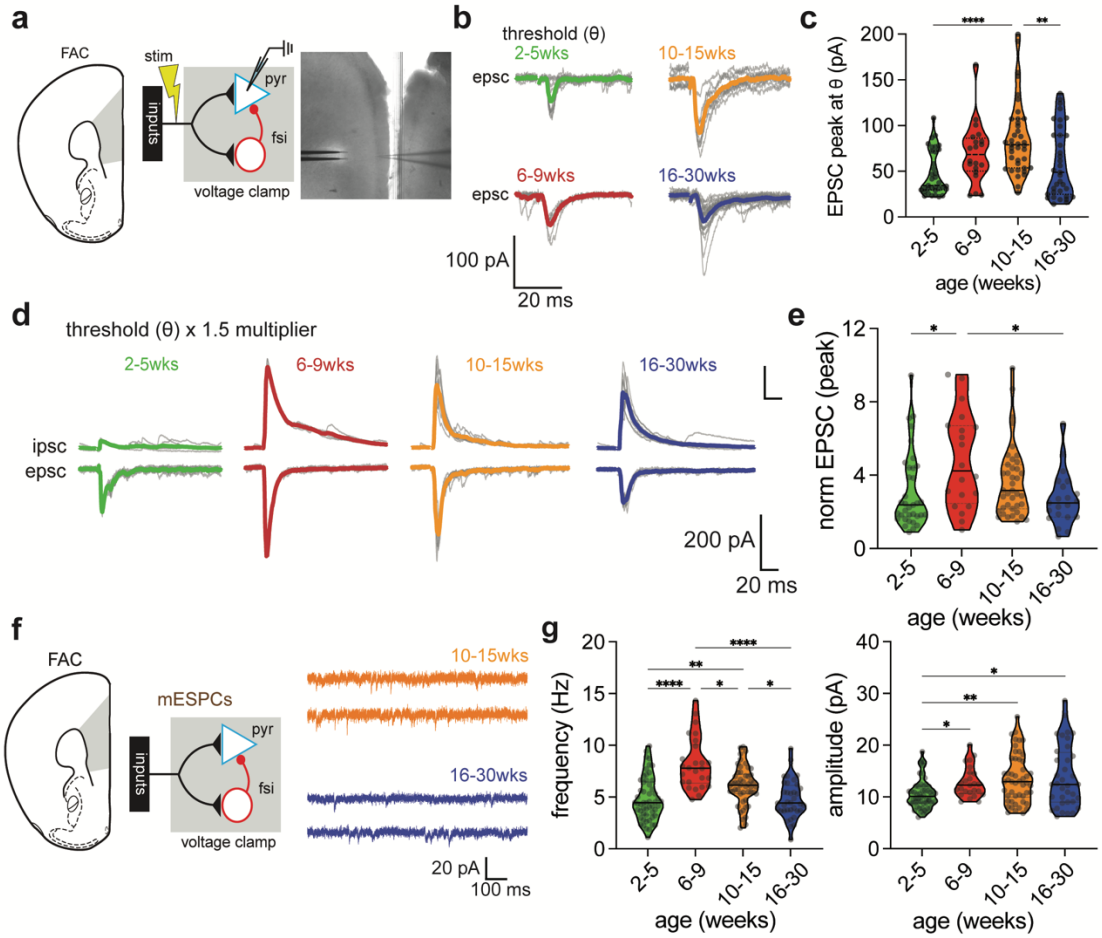

671

672 **Figure 2. Refinement of excitatory drive onto l2/3 pyramidal (pyr) neurons in the FAC**

673 **a,** Schematic of stimulation and recording configuration for analyzing evoked synaptic currents
674 in l2/3 pyramidal (pyr) neurons with (inset, *left*) low-magnification image of stimulator (two-
675 prong) and recording electrode in frontal association cortex (FAC). The bipolar concentric
676 electrode was placed 500 µm from pia (inset, right)

677 **b,** Representative (gray) and average (overlaid color) of evoked EPSCs at threshold (theta) for
678 an individual l2/3 pyr neuron for each age range.

679 **c,** Evoked EPSC peak amplitude in l2/3 pyr neurons at threshold shown as violin plots (solid
680 line=median, dashed line=upper and lower quartiles) with all points superimposed. For EPSC:
681 ($n_{2\text{-}5wks}$=47, $n_{6\text{-}9wks}$=20, $n_{10\text{-}15wks}$=31, $n_{16\text{-}30wks}$=21 cells). One-way ANOVA was performed and
682 found no difference at threshold (Kruskal Wallis test statistic=5.803; p=0.1216

683 **d,** Representative (gray) and average (overlaid color) trials of electrically-evoked EPSCs (V_{hold}=-
684 70 mV) and IPSCs (V_{hold}=0 mV) for an individual l2/3 pyr neuron in each age group

685 **e,** EPSC peak amplitudes evoked at 1.5*threshold in each age group shown as violin plots
686 (solid line=median, dashed line=upper and lower quartiles) with all points superimposed ($n_{2\text{-}5wks}$=47, $n_{6\text{-}9wks}$= 20 cells, $n_{10\text{-}15wks}$=31, $n_{16\text{-}30wks}$=21 cells). One-way ANOVA was performed
687
688 (Kruskal-Wallis statistic=10.49: p=0.0148) with tests for multiple comparisons (* p<0.05)

f, Schematic of configuration for recording miniature excitatory postsynaptic current (mEPSC) from l2/3 pyr neurons and representative traces of mEPSC recordings from pyr neurons at two of the four ages analyzed.

g, Frequency (left) and amplitude (right) of mEPSCs in l2/3 pyr neurons from each age group shown as violin plots (solid line=median, dashed line=upper and lower quartiles) with all points superimposed ($n_{2\text{-}5wks}$=54, $n_{6\text{-}9wks}$ =33, $n_{10\text{-}15wks}$=51, $n_{16\text{-}30wks}$=36 cells). For frequency: one-way ANOVA was performed (Kruskal Wallis test statistic=40.48; $p<0.0001$) with tests for multiple comparisons (* $p<0.02$, ** $p=0.0089$, **** $p<0.0001$). For amplitude: one-way ANOVA was performed (Kruskal Wallis test statistic=15.79; $p=0.0013$) with tests for multiple comparisons (* $p<0.03$, ** $p<0.004$)

Figure 3

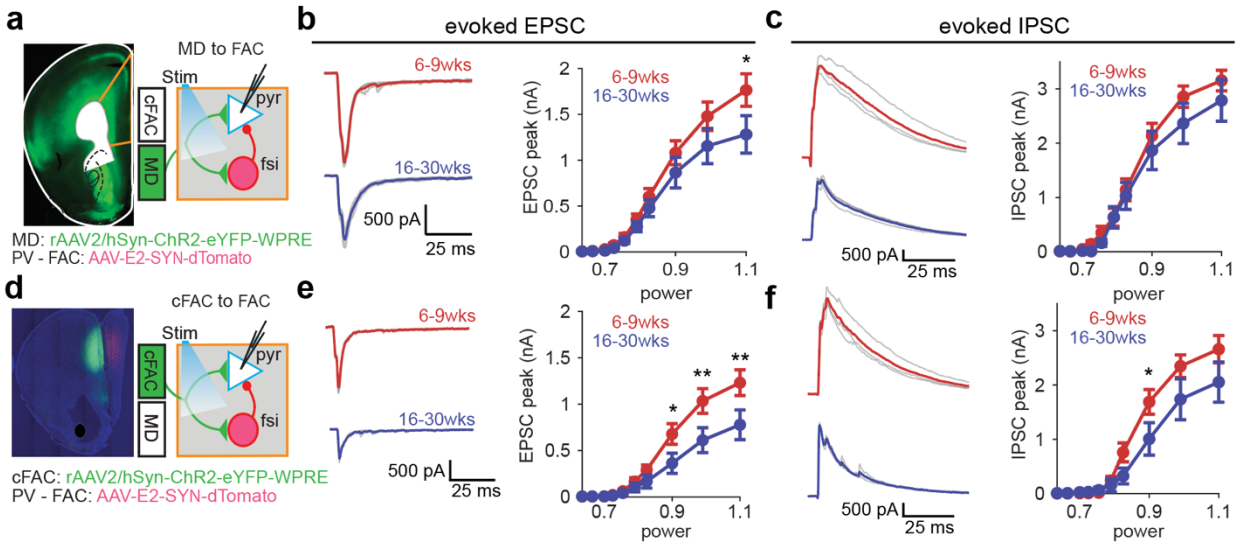

Figure 3. Differential age-dependent refinement of cortical vs. thalamic excitatory drive onto l2/3 pyramidal neurons

a, Schematic of experimental preparation showing low-magnification image of expression of ChR2-YFP in mediodorsal thalamic (MD) axons in the FAC (*left*) and recording configuration (*right*).

b, Representative traces (*left,* average overlaid) (V_{hold}=-70 mV) and peak amplitude of optically-evoked thalamic EPSCs in l2/3 pyrs as a function of laser power in two age groups ($n_{6\text{-}9wks}$=31, $n_{16\text{-}30wks}$=19 cells). Average +/- standard error of the mean shown. Two-way repeated measures ANOVA was performed (p=0.186) with tests for multiple comparisons (* p<0.02)

c, As in panel **b** but for polysynaptic inhibitory postsynaptic currents (IPSCs) (V_{hold}=0 mV) ($n_{6\text{-}9wks}$=31, $n_{16\text{-}30wks}$=19 cells). Two-way repeated measures ANOVA was performed (p=0.3487).

d, Schematic of experimental preparation showing low-magnification image of expression of ChR2-YFP in cFAC and expression of the red fluorophore in the FSIs (*left*) and recording configuration (*right*).

e, As in panel **b** but for optically-evoked cortical inputs to l2/3 pyrs ($n_{6\text{-}9wks}$=19, $n_{16\text{-}30wks}$=17 cells). Two-way repeated measures ANOVA was performed (p=0.053) with tests for multiple comparisons (* p=0.038, ** p<0.002)

f, As in panel **c** but for polysynaptic IPSCs recorded in l2/3 pyrs and evoked by optical stimulation of cortical inputs ($n_{6\text{-}9wks}$=19, $n_{16\text{-}30wks}$=17 cells)**.** Average +/- standard error of the mean shown. Two-way repeated measures ANOVA was performed (p=0.122) with tests for multiple comparisons (* p=0.0487)

Figure 4

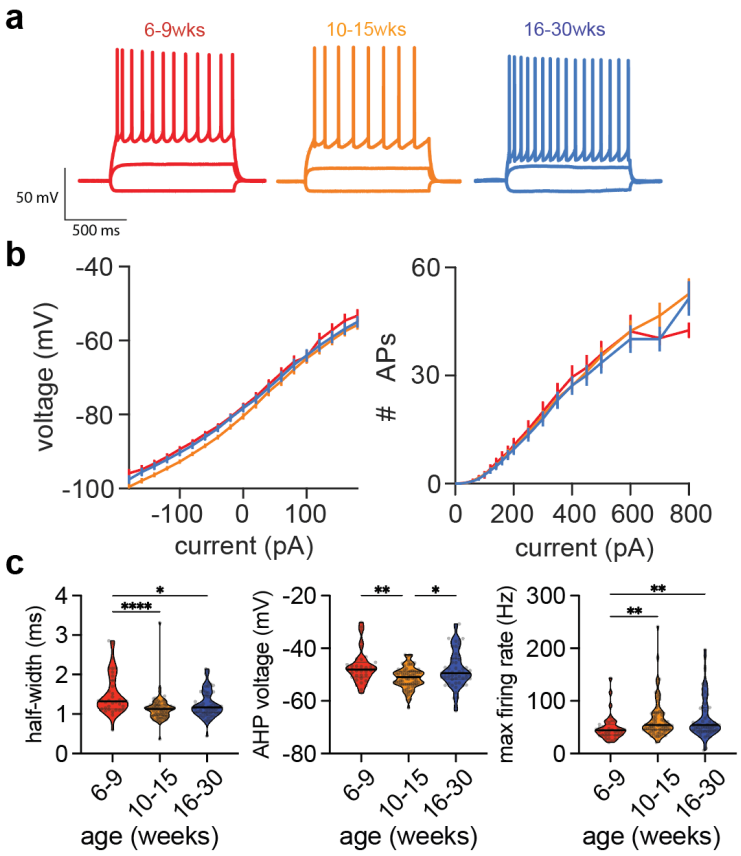

725

726 **Figure 4. Intrinsic properties and excitability across age**

727 **a,** Representative traces of whole-cell currant clamp recordings of l2/3 pry neurons in the
728 presence of synaptic blockers at each indicated age range. The color code is maintained
729 throughout the figure.

730 **b,** Plateau voltage (*left*) and action potential firing rate (*right*) vs. amplitude of current step (1 s, -
731 200 to 800 pA) for each age group as indicated in panel **a**

732 **c,** Action potential half-width (*left*), afterhyperpolarization (AHP) voltage (*middle*), and maximum
733 firing rate (FR_{max}, *right*) as a function of current step amplitude for each age group shown as
734 violin plots (solid line=median, dashed line=upper and lower quartiles) with all points
735 superimposed ($n_{6\text{-}9wks}$=35, $n_{10\text{-}15wks}$=71, $n_{16\text{-}30wks}$ =55 cells). For half-width: one-way ANOVA was
736 performed (Kruskal Wallis test statistic=19.17; p<0.0001) with tests for multiple comparisons (*
737 p=0.0239, **** p<0.0001). For AHP voltage: one-way ANOVA was performed (Kruskal Wallis
738 test statistic=12.72; p=0.0017) with tests for multiple comparisons (* p=0.0340, ** p=0.0031).
739 For FR_{max}: one-way ANOVA was performed (Kruskal Wallis test statistic=11.18; p=0.0037) with
740 tests for multiple comparisons (* p<0.01)

741

Figure 5

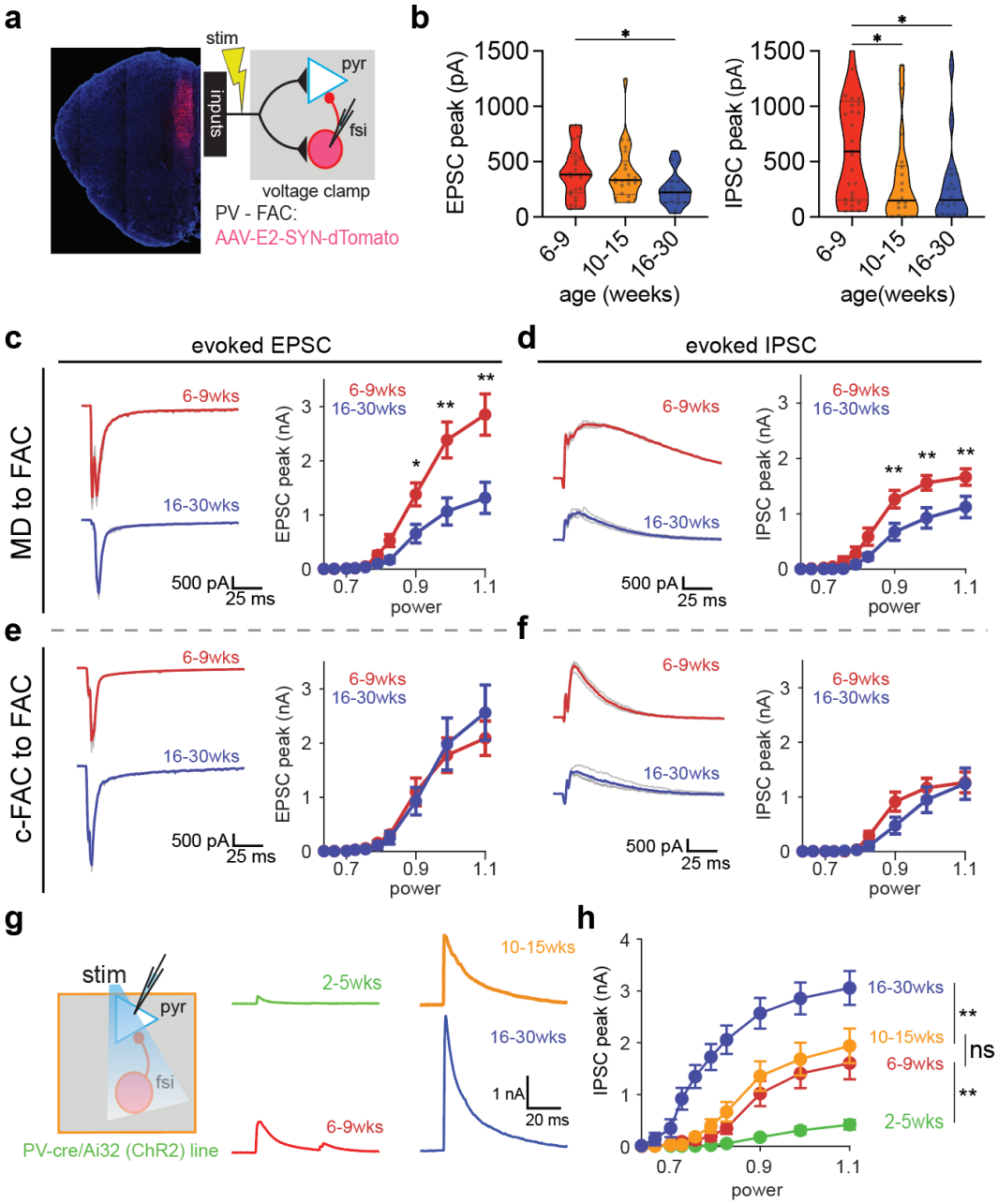

Figure 5. Differential age-dependent refinement of cortical vs. thalamic excitatory drive onto l2/3 fast-spiking interneurons

a, Schematic of stimulation and recording configuration for analyzing evoked synaptic currents in fast-spiking interneurons (FSIs) with (inset, *left*) low-magnification image of AAV expression driving fluorophore in putative FSIs in the FAC. The bipolar concentric electrode was placed 500 µm from pia.

b, Evoked synaptic current peak at 1.5*threshold shown for EPSCs (*left*) and IPSCs (*right*) across ages ($n_{6\text{-}9wks}$=29, $n_{10\text{-}15wks}$=22, $n_{16\text{-}30wks}$=18 cells) shown as violin plots (solid line=median,

751 dashed line=upper and lower quartiles) with all points superimposed. Two-way repeated
752 measures ANOVA was performed (p=0.0328) with tests for multiple comparisons (* p=0.034).

753 **c,** Representative traces (*left,* average overlaid) (V_{hold}=-70 mV) and peak amplitude of optically-
754 evoked thalamic EPSCs in l2/3 pyrs as a function of laser power in two age groups ($n_{6\text{-}9wks}$=15,
755 $n_{16\text{-}30wks}$=20 cells). Average +/- standard error of the mean shown. Two-way repeated measures
756 ANOVA was performed (p=0.002) with tests for multiple comparisons (* p=0.010, ** p<0.0001).

757 **d**, As in panel **c** but for polysynaptic IPSCs recorded in FSIs (V_{hold}=0 mV) ($n_{6\text{-}9wks}$=15, $n_{16\text{-}}$
758 $_{30wks}$=20 cells). Two-way repeated measures ANOVA was performed (p=0.002) with tests for
759 multiple comparisons (** p<0.0008).

760 **e,** As in panel **c** but for optically-evoked cortical inputs to FSIs ($n_{6\text{-}9wks}$=19, $n_{16\text{-}30wks}$=17 cells).
761 Two-way repeated measures ANOVA was performed (p=0.814).

762 **f**, As in panel **e** but for polysynaptic IPSCs recorded in FSIs and evoked by optical stimulation of
763 cortical inputs ($n_{6\text{-}9wks}$=19, $n_{16\text{-}30wks}$=17 cells). Two-way repeated measures ANOVA was
764 performed (p=0.318).

765 **g,** Schematic of optogenetic stimulation and recording configuration in tissue expressing ChR2
766 in PV+ FSIs in FAC (*left*) and representative traces (average overlaid) of evoked IPSCs (each
767 cell was held at 0 mV) onto l2/3 pyramidal (pyr) neurons (*right*) in l2/3 pyr neurons at a variety
768 of ages.

769 **h,** Evoked synaptic current peak from low to high laser power in l2/3 pyr neurons across ages
770 ($n_{2\text{-}5wks}$=41, $n_{6\text{-}9wks}$=21, $n_{10\text{-}15wks}$= 18, $n_{16\text{-}30wks}$=9 cells)**.** Average +/- standard error of the mean
771 shown. Two-way repeated measures ANOVA was performed (p<0.0001) with tests for multiple
772 comparisons (NS p=0.372, ** p<0.0001)

773

Figure 6

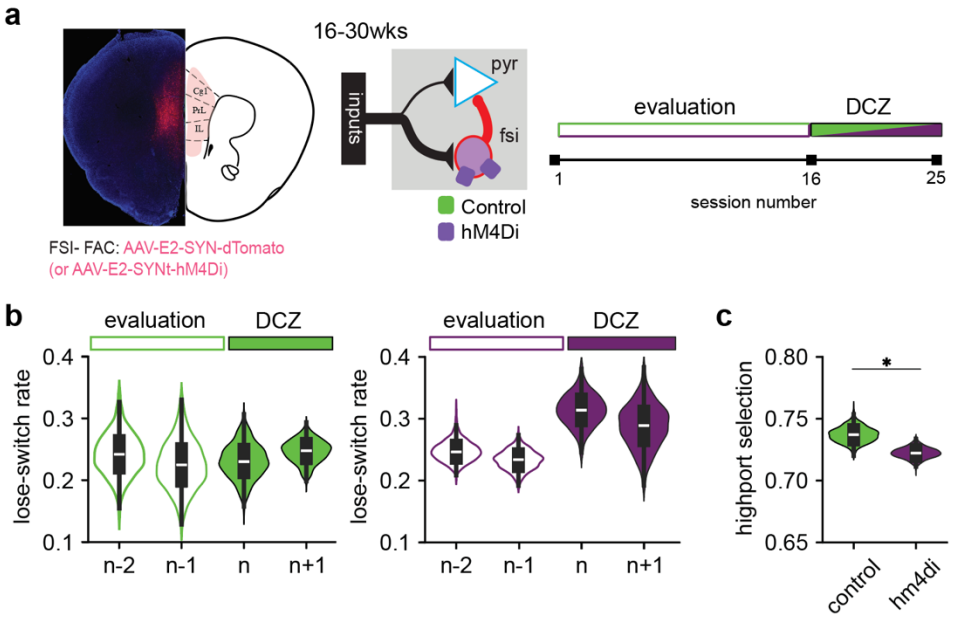

774

775 **Figure 6. Decreased inhibition reverses age-related changes in 2-armed bandit task**

776 **a,** Representative image (inset, *left*) of frontal association cortical (FAC) expression of AAV
777 driving either fluorophore (dTomato) or inhibitory DREADDs receptor (HM4Di) under the
778 synapsin (SYN) promotor and with the putative fast spiking interneuron (FSI) enhancer (E2).
779 Schematic of receptor expression (inset, *right*) in FSIs and not in pyramidal neurons. Schematic
780 of experimental timeline (*right*): 15 sessions of evaluation without drug administration followed
781 by 10 sessions with administration of DCZ (1-3 mg/ml) via intraperitoneal injection 30-minutes
782 prior to each session.

783 **b,** Bootstrapped distributions of the lose-switch rate for control fluorophore (*left*) and hM4Di
784 (*right*) expression animals before (unfilled; n-2, n-1) and after (filled; n, n+1) the start of the
785 sessions with DCZ administration (session n).

786 **c,** Bootstrapped distribution of highport selection rate in the final five sessions of DCZ
787 administration in hM4Di and control flourophore expressing mice.

788

789 **Supplementary Figures**

Supplementary Figure 1

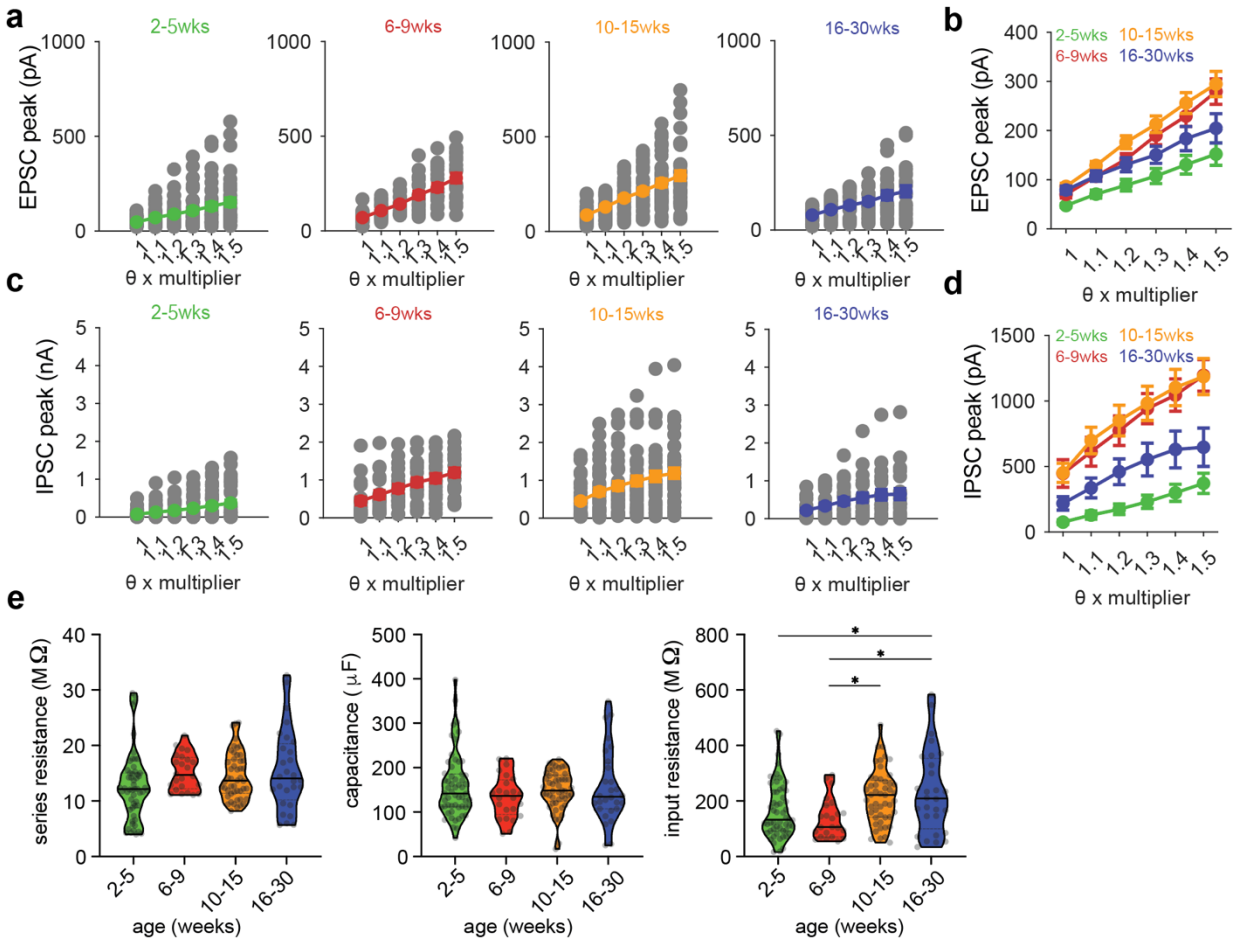

790

791 **Supplementary Figure 1 Protracted development of excitatory and inhibitory drive onto**
792 **l2/3 pyramidal (pyr) neurons in the frontal association cortex (FAC)**

793 **a,** Evoked synaptic current peak from threshold to threshold x 1.5 multiplier shown for excitatory
794 (EPSC) postsynaptic currents onto l2/3 pyr neurons (grey=individual cells overlaid with average)
795 across ages ($n_{2\text{-}5wks}$=47, $n_{6\text{-}9wks}$=20, $n_{10\text{-}15wks}$=31, $n_{16\text{-}30wks}$=21 cells).

796 **b,** Averaged evoked synaptic current peak from threshold to threshold x 1.5 multiplier across
797 ages. Average +/- standard error of the mean shown. Two-way repeated measures ANOVA was
798 performed (p=0.052) with tests for multiple comparisons (* p=0.007).

799 **c,** As in panel **a** but for polysynaptic inhibitory postsynaptic currents (IPSCs) onto l2/3 pyr
800 neurons (V_{hold}=0 mV).

801 **d,** As in panel **b** but for the average polysynaptic inhibitory postsynaptic currents (IPSCs)
802 (V_{hold}=0 mV) onto l2/3 pyr neurons ($n_{2\text{-}5wks}$=47, $n_{6\text{-}9wks}$=20, $n_{10\text{-}15wks}$=31, $n_{16\text{-}30wks}$=21 cells).

803 **e,** Series resistance (left), capacitance (μF) (middle) and Input resistance (right) shown as violin
804 plots (solid line=median, dashed line=upper and lower quartiles) with all points superimposed
805 ($n_{2\text{-}5wks}$ =54, $n_{6\text{-}9wk}$=33, $n_{10\text{-}15wks}$=51, $n_{16\text{-}30wks}$=36 cells). **All cells included from electrical**
806 **stimulation experiment, even those where stimulation led to greater than 250 pA**

excitatory response. For series resistance: one-way ANOVA was performed (F-statistic=2.37; p=0.0790). For capacitance: one-way ANOVA was performed (F-statistic=0.9209; p=0.4428). For input resistance: one-way ANOVA was performed (F-statistic =5.168; p=0.0020) with tests for multiple comparisons (* $p<0.02$, ** $p<0.3$ ** $p<0.004$).

Supplementary Figure 2

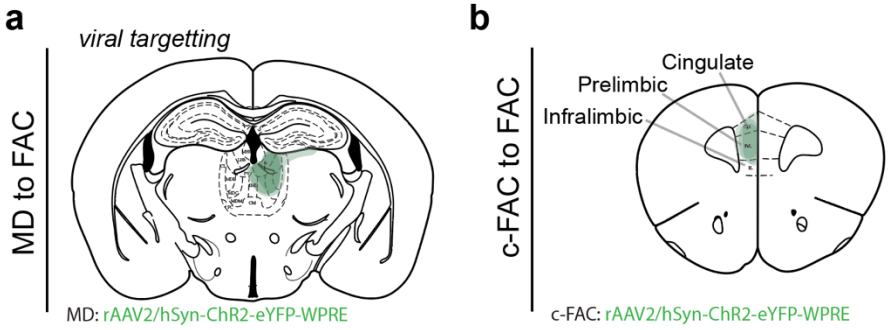

Supplementary Figure 2 Targeting location for optogenetic-assisted mapping of mediodorsal thalamic and contra-frontal cortical inputs

a, Representative viral targeting location across 3 animals in the mediodorsal thalamus (MD), injected with the AAV driving expression of channelrhodopsin (ChR2) in neurons (human synapsin (hSyn) promoter)

b, Representative viral targeting location across 3 animals in the contralateral-frontal association cortex (c-FAC), injected with the AAV driving expression of ChR2 in neurons (hSyn promoter)

Supplementary Figure 3

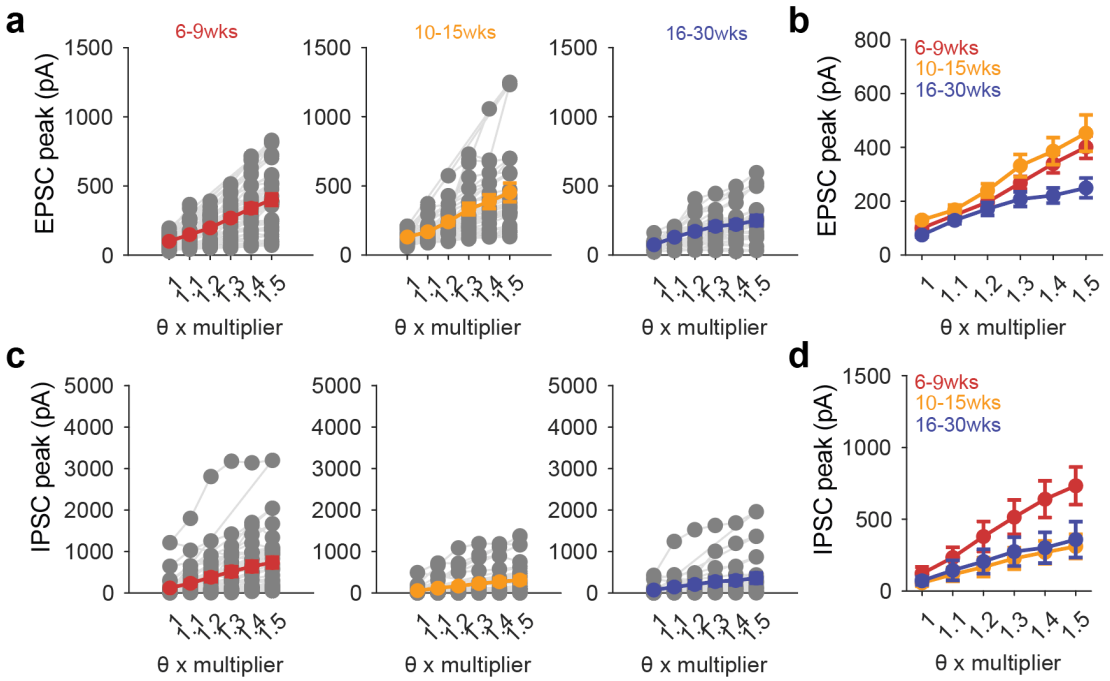

Supplementary Figure 3 Protracted development of excitatory and inhibitory drive onto fast-spiking interneurons (FSIs) in the frontal association cortex (FAC)

a, Evoked synaptic current peak from threshold to threshold x 1.5 multiplier shown for excitatory (EPSC) postsynaptic currents onto FSIs (grey=individual cells overlaid with average) across ages ($n_{6\text{-}9wks}$=29, $n_{10\text{-}15wks}$=22, $n_{16\text{-}30wks}$=18 cells).

b, Averaged evoked synaptic current peak from threshold to threshold x 1.5 multiplier across ages. Average +/- standard error of the mean shown.

c, As in panel **a** but for polysynaptic inhibitory postsynaptic currents (IPSCs) onto FSIs (V_{hold}=0 mV).

d, As in panel **b** but for the average polysynaptic inhibitory postsynaptic currents (IPSCs) (V_{hold}=0 mV) onto FSIs ($n_{6\text{-}9wks}$=29, $n_{10\text{-}15wks}$=22, $n_{16\text{-}30wks}$=18 cells).

Supplementary Figure 4

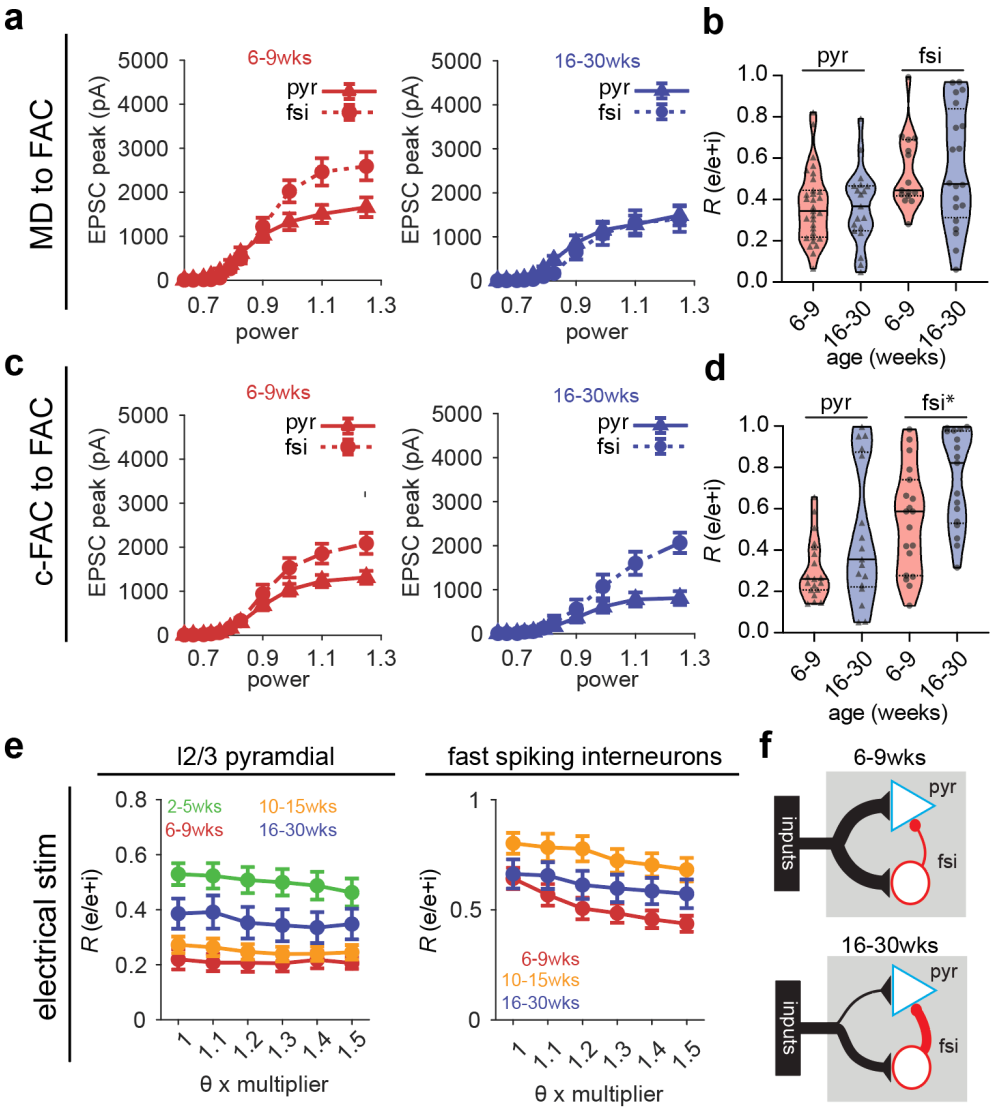

Supplementary Figure 4 Protracted refinement of excitatory/inhibitory balance drive onto l2/3 pyramidal neurons and fast spiking interneurons across experimental paradigms

a, Optically-evoked mediodorsal (MD) thalamic EPSCs onto l2/3 pyramidal (pyr) neurons and fast-spiking interneurons (FSIs) as a function of laser power at 6-9 weeks (left) and 16-30 weeks (right). Average +/- standard error of the mean shown.

b, Fraction of EPSC over total synaptic inputs (EPSC+IPSC) onto l2/3 pyr (left) and FSIs (right) vs. the optogenetic stimulation of MD inputs across the two ages shown as violin plots (solid line=median, dashed line=upper and lower quartiles) with all points superimposed (pyr: $n_{6\text{-}9wks}$=31, $n_{16\text{-}30wks}$=19 cells & fsi: $n_{6\text{-}9wks}$=15, $n_{16\text{-}30wks}$=20 cells).

c, As in panel **a** but for optically evoked contracortical (c-FAC) inputs onto currents l2/3 pyr neurons and FSIs at 6-9 weeks (left) and 16-30 weeks (right).

d, Fraction of EPSC over total synaptic inputs (EPSC+IPSC) onto l2/3 pyr (left) and FSIs (right) vs. the optogenetic stimulation of c-FAC inputs across the two ages shown as violin plots (solid

849 line=median, dashed line=upper and lower quartiles) with all points superimposed (pyr: n_{6-9wks}=19, $n_{16-30wks}$=17 cells, fsi=(n_{6-9wks}=19, $n_{16-30wks}$=17 cells).

851 **e,** As in panel **b** but for electrically evoked synaptic currents for l2/3 pyr neurons (left) and FSIs
852 (right)

853 **f,** Schematic representation of observed changes onto l2/3 pyr neurons and FSIs through
854 analysis of excitatory and inhibitory postsynaptic currents (EPSCs & IPSCs, respectively).

855

Supplementary Table

stage	decision window	p(high port)	p(low port)	blocklength
1	NA	1.0	1.0	NA
2	15	1.0	0.0	50
3	7	1.0	0.0	50
4	3	1.0	0.0	50
5	2	1.0	0.0	30
6	2	1.0	0.0	20
7	2	0.8	0.2	10-30

Supplementary Table 1: Stages of acquisition for the 2-armed bandit task (2-ABT)

Center poke followed by a side poke behavior is shaped over the course of 6 stages where experimenter shifts the amount of time to make center to side selection (‘decision window’ in seconds), probability of the highly rewarded (p(high port)) and lowly rewarded (p(low port)) ports and the length of trials that the rule is held constant (‘blocklength’). Stage 7 represents the final stage of the 2-ABT that is used for the execution phase.